# Engineered refractive and diffractive optical composites via photo-thermal processes

## P. S. SHIRSHNEV,* M. KANG, I. DIVLIANSKY, K. A. RICHARDSON, AND L. B. GLEBOV

*College of Optics and Photonics, CREOL, University of Central Florida, 4304 Scorpius Street, Orlando, Florida 32816, USA*

*pavel.shirshnev@ucf.edu*

**Abstract:** Oxide and non-oxide glass with tailored morphology or microstructure induced by photo-exposure and subsequent heat treatment can result in new materials with unique optical functions. Spatial control of where this local modification occurs can result in optical materials with refractive or diffractive behavior different from those found in homogeneous optical materials. We review the use of such strategies to introduce such unique optical function to commercially developed oxide and prototype chalcogenide glass ceramic media that have yielded a range of performance attributes that make them unique in applications requiring reduced size, weight, power and cost (SWAP-C). We summarize how these materials have been designed and created to yield components that combine multiple functions in a single optical element, resulting in unique performance solutions for a variety of optical systems, highlighting the future potential these materials offer.

## 1. Introduction: diffractive and gradient optical elements

For centuries, elements that enable transformation of optical beams have been fabricated from transparent materials with high spatial homogeneities of the refractive index. Typically, desirable beam transformation has been produced by a variation in the spatial profile of optical path ($n \times t$), where $n$ is refractive index and $t$ is thickness. Such spatial profiling of the optical path has been most commonly produced by physical shaping of an element's surface, often through physical material removal made possible by grinding and polishing. Shaping with low spatial frequencies results in refractive (e.g. lenses) or reflective (e.g. mirrors) elements. Shaping with high spatial frequencies results in diffracting elements (e.g. diffraction gratings). A relatively new approach was demonstrated during the last century when spatial profiling of the optical path was produced by the creation of spatial variations of the refractive index. Examples of how such profiling can be produced by several techniques, such as via gradient thermal treatment, ion exchange, multilayer deposition, or ion implantation, has been discussed most recently in a review on visible and infrared refractive index modification methods and their limitations [1].

This survey describes specific materials that provide spatial refractive index variations by photo-thermo-induced precipitation of crystalline phases in vitreous materials and properties of refractive and diffractive elements produced with this technique. Silicate and chalcogenide glasses with transparency from the UV to long wavelength IR region are considered along with gradient lenses, thin and volume diffractive gratings, and complex holographic elements produced from these materials.

## 2. Silicate-based photo-thermo-refractive (PTR) glass

The story started in 1949 when Corning Glass Work announced photosensitive glass as a new type of photographic media [2]. Here, the photographic process based on photo-thermo-induced absorption resulted from different crystalline phases precipitating in an ultraviolet (UV) radiation

exposed glass. This multicomponent oxide glass matrix comprised of $SiO_2$-$Na_2O$-$Al_2O_3$-$ZnO$ also included F and Br, along with such sensitizers as $Ag^+$, $Ce^{+3}$, $Sn^{+2}$, $Sb^{+3}$. Forty years later, it was found that UV exposure followed by thermal precipitation of the crystalline phase of $Li_2SiO_3$ produced refractive index change and the first volume phase hologram in inorganic glass was recorded [3]. The use of glass similar to described in Ref. [2] with precipitation of NaF resulted in dramatic decrease of optical losses and recording of high efficiency volume holographic elements [4,5]. Glasses, where phase holograms are recorded by refractive index change after exposure of optical radiation followed by thermal treatment were thus defined as "photo-thermo-refractive" (PTR) glasses.

The classical composition of PTR glass is a sodium-potassium-zinc-aluminum-fluorine-bromine silicate glass doped with antimony, tin, cerium, and silver. The photo-thermal-refractive process in PTR glass is based on precipitation of dielectric nanocrystals of NaF in the bulk of glass exposed to UV radiation [6]. The process results in a refractive index change that can be described in several steps, as presented in [7]. Before thermal development of the glass, the material is totally vitreous [8]. The first step involves the UV exposure of glass by radiation of light with wavelength λ, where $350\,nm > \lambda > 250\,nm$ within the absorption band of $Ce^{3+}$ produces photoionization of a cerium ion converting it to $Ce^{4+}$ (Fig. 1).
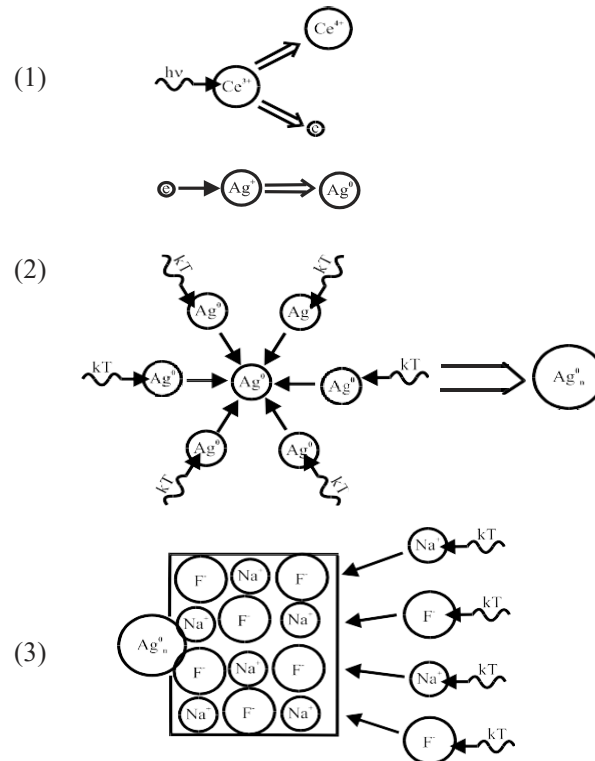


**Fig. 1.** Stages of photo-thermo-crystallization [7].

The released electron(s) are then trapped by intrinsic defects of the glass matrix or dopants in their highest valence state, including $Sb^{+5}$ and $Ag^+$. Trapping electrons by $Ag^+$ ions converts the species to $Ag°$. UV-exposed glass is then nucleated at temperatures between 450 and 500°C, and here, silver atoms agglomerate and form colloidal silver containing particles, most probably, silver bromide clusters [9]. These silver-containing particles serve as nucleation centers for subsequent sodium fluoride crystal growth at temperatures between 500 and 550°C. Sodium fluoride crystal

growth on top of the silver (or silver bromide) clusters can be controlled by the diffusion rate (defined by the development temperature) of sodium and fluorine from the glass matrix, to the crystals. After this last step, the local refractive index of the exposed area decreases by about $10^{-3}$ compared to that in the unexposed area. While the process of photo-thermo-crystallization is clear and exhibits a linear correlation of refractive index change with volume fraction of NaF crystalline phase [6], the exact mechanisms of refractive index change are still under discussions [10,11] and require additional research.

The region of photosensitivity in PTR glass is determined by the absorption band of $Ce^{3+}$ with a maximum at 305 nm and ranges from approximately 280 to 350 nm. The main parameter that allows description of a photosensitive material is the refractive index kinetics, i.e. the evolution of the photo-induced refractive index change as a function of the magnitude of irradiation dose. The refractive index change is controlled by three interconnected parameters: the dosage of UV-exposure, the thermal treatment temperature and duration. Dependence of the refractive index decrement on dosage at 325 nm for different times of thermal development is shown in Fig. 2 [8].
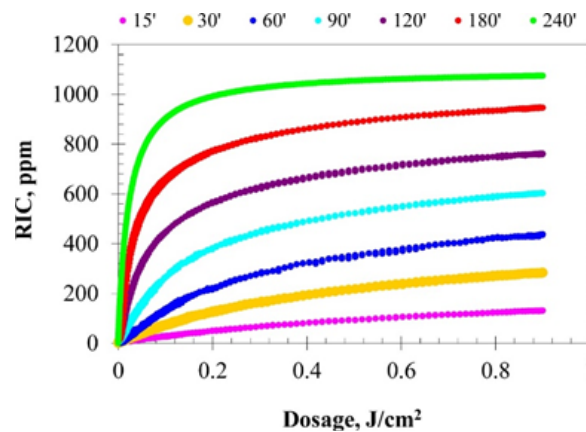


**Fig. 2.** Dependence of the refractive index change (RIC) in PTR glass on dosage of UV-exposure after thermal treatment at ~515°C for different durations (top) [8].

An induced refractive index exhibits a curve with a continuously decreasing slope which is described by hyperbolic functions [12]. An increase in the time of development increases the initial slope while a saturation level is the constant. It was found that refractive index decrement does not depend on the power density of exciting radiation. This means that PTR glass obeys the Reciprocity Law and the induced index of refraction depends on the total dosage only [13]. The maximum value of the refractive index decrement in experiments was about $10^{-3}$.

An absorption in PTR glass is determined by the initial absorption of the original glass and by induced absorption caused by photo-induced reactions. The absorption spectrum of the virgin PTR glass is presented in Fig. 3, left. The window of complete transparency extends from 350 to 2700 nm. The glass' absorption edge in the UV region is formed by bands of cerium. Absorption at wavelengths greater 2700 nm is produced by both hydroxyl groups and the glass matrix [7].

The near IR absorption coefficients in virgin PTR glass range from $5 \times 10^{-5}$ to $2 \times 10^{-4}$ cm$^{-1}$. This absorption is an order of magnitude lower compared to that of conventional optical glasses (e.g. BK7) [14]. PTR glass does not have detectable intrinsic absorption in the near-IR spectral region [15]. The residual near-IR absorption in such glasses is caused by different types of impurities, as illustrated in Fig. 3, right. The most probable reason for absorption in the vicinity of 1 µm is due to residual contamination by iron and hydroxyl groups. Variations in the absorption
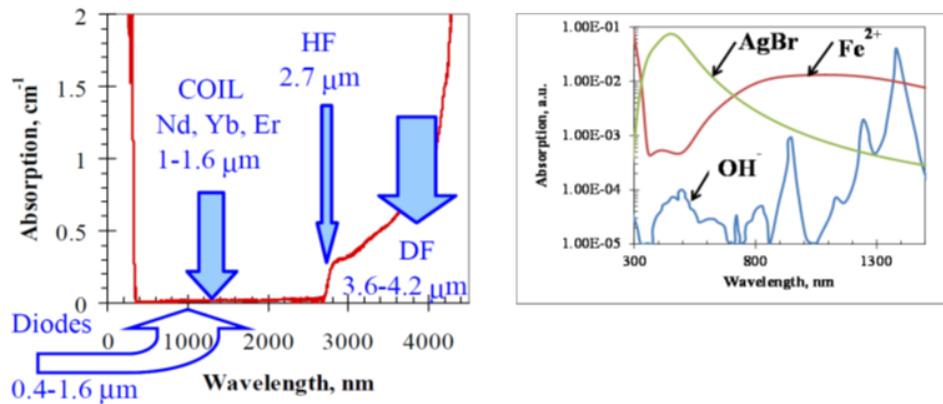
**Fig. 3.** Absorption spectrum of virgin PTR glass (left) [7]. Arrows show wavelengths of most common lasers operation range. Absorption spectra (not in scale) of the main absorbing species in PTR glasses (right) [16].

coefficient at 1 μm could be caused both by differences in the total concentration of iron and redistribution between different valence states of $Fe^{2+}$ and $Fe^{3+}$ [16].

The fabrication of volume Bragg gratings (VBGs) in PTR glass results from UV exposure followed by thermal treatment that induce additional losses. Here, the thermal development of UV-exposed PTR glass generates silver containing particles that participate in the nucleation process. Those particles have absorption band whose position and width may vary from 400 to 600 nm depending on the size distribution and on the presence of halides [17,18]. Typical losses for the UV-exposed (4 J/cm$^2$ at 325 nm) and thermally developed (1 h at 515°C) PTR glass are shown in Fig. 4 (line (2)).
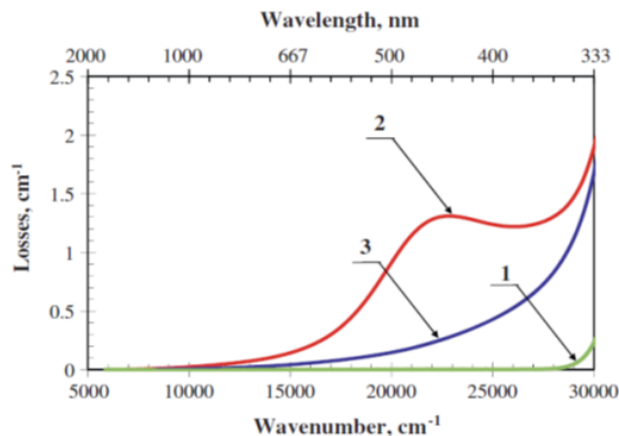


**Fig. 4.** Spectra of total internal loss in a PTR glass sample. (1) Original absorption spectrum, (2) after exposure to UV radiation at 325 nm for 4J/cm$^2$ and development for 1 h at 515 °C, (3) after additional bleaching by visible radiation at 532 nm [18].

In the UV region, it is the superposition of the absorption of the original glass, mainly a combination of $Ce^{3+}$ and $Ce^{4+}$ absorption bands [19], absorption of silver containing particles, color centers, and scattering [20] that result in the spectrum shown. In the visible and near-IR ranges, the main contributions are from induced absorption of silver containing particles and

scattering. An absorption band with a maximum in the 400-500 nm range is associated with the plasmon resonance of silver particles. Its exponential tail extends to the near-IR range. It was shown [21], that induced absorption of silver containing particles can be completely bleached by the second harmonic of a Nd:YAG laser at 532 nm. Scattering in virgin PTR glass is being about two times higher than that in fused silica. Scattering in processed PTR glass results from precipitation of the microcrystalline phase of NaF [18] (Fig. 4, curve 3).

A long wavelength absorption edge in PTR glass starts at 2700 nm [7]. Decimal absorption coefficient (internal optical density/thickness) gradually increases from 0.2 to 1 cm$^{-1}$ in the range of 2800-4000 nm. This absorption has been ascribed to an admixture of hydroxyl groups. To extend the operational window of PTR glass to longer wavelengths, a new type of PTR glass was melted known as dehydrated glass. Dehydrated glass was melted under a fused silica dome with dry air purging [22]. The dehydrated glass technology allowed a further decrease in absorption coefficient at 2800 nm, down to 0.04 cm$^{-1}$. The absorption spectra of dehydrated (D) and regular (R) PTR glass are shown on the Fig. 5. A comparative study of glasses containing different concentration of water allowed deconvolution of the absorption spectra of water and the glass' matrix. The absorption edge parameters for PTR glass matrix which set the limits for near IR applications of PTR glass were defined. The absorption coefficient is 0.01 cm$^{-1}$ for 2900 nm and 0.1 cm$^{-1}$ for 3600 nm.
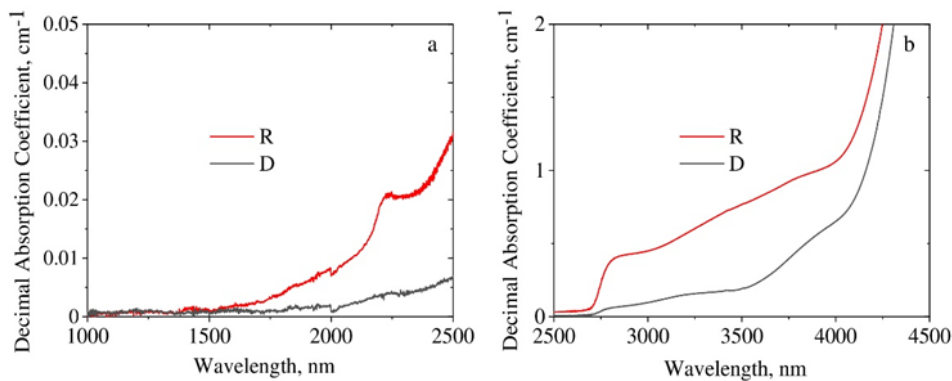


**Fig. 5.** Absorption spectra of dehydrated (D) and regular (R) PTR glass [22] within the range 1000-2500 nm (a) and 2500-4500 nm (b).

Holographic elements in PTR glass can withstand multi-kilowatt laser beams. Focusing of a continuous wave (CW) laser beam by a small spot of about 300 μm and power density of 100 kW/cm$^2$ demonstrated that no fading of the hologram was observed after such illumination [7].

Testing of PTR diffractive grating under irradiation with a 4 kW Yb fiber laser focused to a 4 mm diameter spot (IPG Photonics, Inc.) showed its stability while heating did not exceed 15 K. It should be noted that brittle fracturing of the grating at 2 kW was caused by a surface defect but not the internal (bulk) glass properties [23]. The laser damage threshold in bulk of PTR glass was found to be in the range of 40 J/cm$^2$ for 8 ns laser pulses at 1064 nm [24]. The surface damage threshold is connected mainly to the quality of optical polishing. The PTR's nonlinear refractive index is 3.3×10$^{20}$ m$^2$/W for 800 nm that is about the same as that of fused silica [25]. Thus, it enables a high tolerance to ultrashort laser pulses. This high laser damage threshold allows the use of PTR diffractive elements in optical systems with any type of high-power pulsed lasers.

New opportunities for PTR glass applications were created by a combination of photosensitivity and luminescent properties. The photosensitive gain media was created by co-doping a regular PTR glass matrix with both photosensitizers (Ce, Ag, Sn and Sb) and a luminescent agent (Nd)

[26]. This new glass shows photoinduced refractive index changes up to $2.5 \times 10^{-4}$, luminescence lifetime of 700 μs, and an emission cross section at 1.06 μm of $1.4 \times 10^{-20}$ cm$^2$. Optical properties of PTR glass co-doped with $Nd^{3+}$ are shown in Fig. 6. A comparative study of spectral-luminescent and laser characteristics of PTR glasses doped with rare earth ions was reported in [27,28].
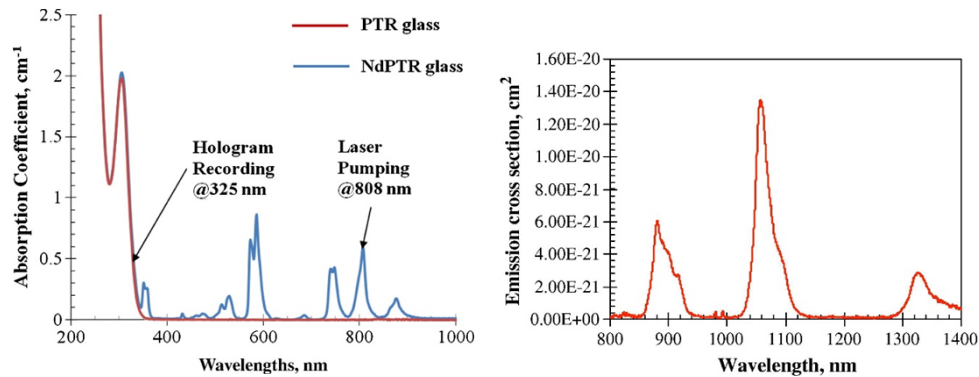


**Fig. 6.** Absorption spectra of PTR and Nd doped PTR glasses (left). Luminescence spectra of Nd doped PTR glass excited with a xenon lamp radiation at $\lambda = 400$ nm (right) [26].

The photosensitivity range of original PTR glass is limited by the UV absorption band of $Ce^{3+}$, located in the 280-350 nm spectral region. As a result, only trivial planar holographic elements, such as volume Bragg gratings, can be recorded in PTR glass for applications in the visible and IR spectral regions. Complex holograms recorded in PTR glass could be used only within the photosensitivity range in near UV. Two approaches have been used to extend PTR glass sensitivity towards longer wavelengths. The first one is to expose an UV-irradiated PTR glass plate to high power pulsed radiation at 532 nm [21]. Obtained partial bleaching of nucleation centers results, after thermal development, in refractive index change according to intensity profile of visible radiation. This means that complex holograms in the visible region could be recorded. The second approach is to dope the PTR glass matrix with terbium. Here, an excited state absorption mechanism was used for the two-step ionization of $Tb^{3+}$ ions by concurrent illumination with long wavelength (449, 522, 808 or 975 nm) and UV (375 nm) beams [29]. Refractive index modulation exceeding $2 \times 10^{-4}$ was observed after exposing the material to blue, green and near IR laser radiation. These results paved a way to recording complex holograms operating in the visible and near IR spectral regions.

## 3.  Chalcogenide photo-thermo-refractive (PTR) glass

As shown above, the use of silicate-based PTR glass in the long wavelength region is limited at 3-3.5 μm because of intrinsic vibrational absorption of the glass matrix. Therefore, non-oxide glasses could be considered for long wavelength operations [30]. Efforts to find a combination of a starting material system and a crystallization-based post modification process have recently resulted in significant progress. Notably, sub-bandgap laser exposure of vapor-deposited multicomponent chalcogenide thin film glasses is one of most successful cases to date [31–34]. When source materials are thermally evaporated and subsequently deposited on a room temperature or cold substrate in the vapor deposition process, they condense at an exceedingly fast rate and become an amorphous film with a high concentration of molecular clusters with strained bonds. Since the strained bonds lower the activation energy required to transform them to a more stable configuration, vapor-deposited chalcogenide thin film glasses are inherently metastable and photosensitive. Specifically, laser exposure with a wavelength near the optical band-edge of

chalcogenide thin film glasses excites lone-pair electrons, with energy states located at the top of the glasses' valence band, to an inter-bandgap energy state [35]. Resulting electron-hole pairs modify the valence of neighboring atoms and reconfigure their molecular bonds [36,37]. The photoionization process induces an increase in the local density of non-bonding atoms and often leads to macroscopic changes in the microstructure such as thermodynamically driven phase separation in a laser-exposed volume.

This photosensitivity has been employed to create unique IR functionalities within $GeSe_2$-$As_2Se_3$-PbSe (GAP-Se) chalcogenide thin films for their use in imaging applications [1, 31–34,38]. Specifically for this GAP-Se material, a photo-thermal process begins with 1064 nm laser exposure of the parent thin films. In these initially homogeneous glass films, 1064 nm laser exposure has been shown to provide the activation energy required to induce the phase separation of the initially homogeneous thin film glass into Pb-rich and Pb-deficient phases both of which remain amorphous and nano-sized. The Pb-rich amorphous phase is energetically unstable, and post thermal treatment at temperatures of 150 - 170°C is sufficient to selectively crystallize the Pb-rich phases and convert them into PbSe or $Ge_{0.1}Pb_{0.9}Se$ nanocrystals, while keeping a surrounding Pb-deficient amorphous matrix [31]. The two-step photo-thermal process is summarized by illustrations as well as corresponding transmission electron microscope (TEM) images and selected area electron diffraction (SAED) patterns in Fig. 7(a) [31].
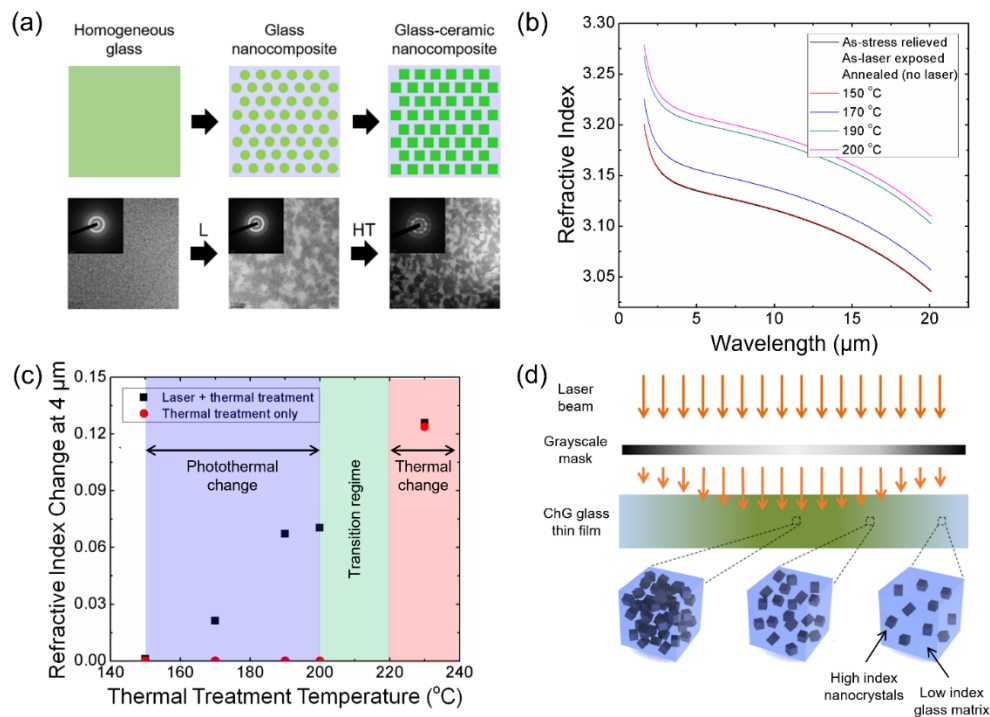


**Fig. 7.** (a) A schematic of microstructural evolution through a photo-thermal process along with corresponding TEM images and SAED patterns. (b) The evolution of refractive index dispersion at each stage of photo-thermal process. (c) A comparison of photo-thermal and thermal-only processes. (d) A photo-thermal process-enabled formation of high refractive index crystals with a spatially varying volume fraction and the corresponding creation of a GRIN profile in a flat optical medium [31]. (a-d) Adapted with permission from [31]. © 2018 Wiley Publishing.

The strong contrast seen in the TEM image and the diffuse rings in the SAED pattern collected from a stage upon laser exposure indicate a phase separation of the starting material into two amorphous phases with two very different weights (i.e., Pb-rich and Pb-deficient). Upon post heat treatment, the TEM image shows that one of the phases develops facets and exhibits asymmetric shapes while the SAED pattern includes crystalline spots as well as previously-seen diffuse rings. These features observed at the final stage of the photo-thermal process indicate the formation of a nanocomposite where Pb-rich crystalline phases such as either PbSe or $Ge_{0.1}Pb_{0.9}Se$ are distributed in a Pb-deficient amorphous matrix.

Since the refractive indices of PbSe or $Ge_{0.1}Pb_{0.9}Se$ nanocrystals (~ 4.9 - 5.0) are far greater than that (~ 2.9) of the amorphous matrix, the photo-thermally-formed high refractive index nanocrystals leads to an increase in the effective refractive index of a resulting glass-ceramic nanocomposite [31–34,39–41]. Figure 7(b) shows the evolution of a target $GeSe_2$-$As_2Se_3$-PbSe chalcogenide thin film's effective refractive index at each stage of the photo-thermal process [31]. Specifically, the refractive index of an as-deposited and stress-relieved film does not change upon laser exposure-only (i.e., with no post thermal treatment) or thermal treatment-only (i.e., no laser exposure). This is because the co-existing phases in an as-laser exposed film are still amorphous (i.e., the absence of high refractive index crystals) and a film which only undergoes a thermal treatment requires temperature greater than a range enabled by laser-induced energetically unstable Pb-rich phases as precursors for crystallization. Post thermal treatment of the laser-exposed film leads to an increase in their refractive index following heat treatment over a temperature range of 150 - 200°C where Pb-rich amorphous phases are exclusively converted into high refractive index PbSe or $Ge_{0.1}Pb_{0.9}Se$ nanocrystals. This occurs without any spontaneous crystallization within the surrounding, unexposed region. Figure 7(c) shows this trend at a wavelength of 4 μm as an example of mid-wave IR (MWIR) range and compares a change made by the photo-thermal process (highlighted with a shade) with that made by the thermal-only process. Key advantages of the photo-thermal process include 1) an ability to increase the effective refractive index of films at temperatures lower than that (> 200°C) required for the thermal-only process and 2) an ability to create high refractive index crystals with a uniform nanoscale diameter thereby maintaining a resulting low loss glass-ceramic as a transmissive effective medium rather than spontaneously nucleated and grown crystals with a large size distribution in the thermal-only process leading to a scattering-induced optical loss [40,41].

While not apparent in Fig. 7(c), another key advantage of the photo-thermal process in GAP-Se is an ability to form a glass-ceramic nanocomposite and achieve a target effective index exclusively within a specific volume of choice thanks to the versatility and spatial resolution of laser beam's movement. While the thermal-only process here involves a large-area "blanket" treatment, the photo-thermal process benefiting from the spatial controllability of the laser exposure process and exclusive conversion of the laser-exposed region to a glass-ceramic nanocomposite medium enables us to "write" a specific spatial profile of refractive index within chalcogenide glass materials. Figure 7(d) shows a representative example of the capability where a laser exposure condition is spatially varied through the insertion of a grayscale optical mask [31]. The spatially-tailored laser exposure and a post thermal treatment would enable a resulting glass-ceramic nanocomposite to exhibit high refractive index nanocrystals with a spatially varying volume fraction. Further to the simple GRIN profile within a single-component flat optical medium illustrated in Fig. 7(d), the spatially-tuned photo-thermal process is expected to create complex spatial profiles of refractive index that would otherwise not be possible with a gradient thermal treatment [39] as well as traditional diffusion-based ion exchange [42] or lamination [43] techniques.

Figure 8(a) shows an ability to systematically tailor the refractive index of $GeSe_2$-$As_2Se_3$-PbSe chalcogenide thin films via a photo-thermal process [31]. Specifically, an increase in laser exposure fluence followed by a fixed heat treatment condition leads to a greater volume fraction

of high refractive index Pb-rich nanocrystals, thereby increasing the effective refractive index of films up to a value of ~ 0.08 at a wavelength of 4 µm. Importantly, the well-defined monotonic relationship of laser exposure fluence and resulting refractive index change allows us to identify a specific laser exposure condition needed to induce a target refractive index change, thereby facilitating a translation of an optical design into device fabrication.
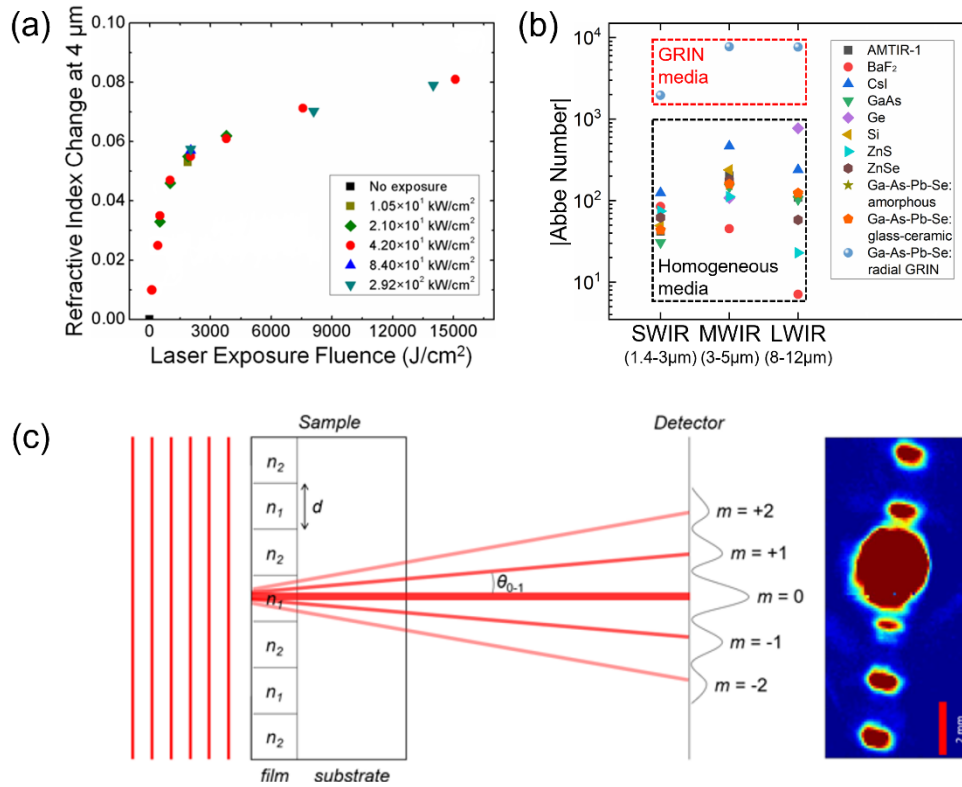


**Fig. 8.** (a) The impact of laser exposure fluence with a fixed post thermal treatment condition on the refractive index of resulting glass-ceramic films at a wavelength of 4 µm. (b) Abbe numbers of various homogeneous and GRIN media. (c) Arrays of photo-thermally-induced glass-ceramic patterns within a glass thin film functioning as a diffraction grating and resulting diffraction spots formed in a transmission mode at a wavelength of 2 µm [31]. (a-c) Adapted with permission from [31]. © 2018 Wiley Publishing.

The ability to engineer the spectral dispersion of a Gradient Index (GRIN) medium is another key aspect, since such a structure would minimize the chromatic aberration of any imaging systems [42]. As an example, we assume a GeSe$_2$-As$_2$Se$_3$-PbSe chalcogenide medium with a radial GRIN profile where a range of its refractive indices over a distance from the center to the edge of the medium corresponds to the range shown in Fig. 8(a). The Abbe number is a number given to describe the extent of an optical material's spectral dispersion [44]. For homogeneous optical media, the Abbe number ($V_{\text{Homo}}$) is formulated by

$$V_{Homo} = \frac{n_{\text{medium}} - 1}{n_{\text{low}} - n_{\text{high}}} \qquad (1)$$

where $n_{low}$, $n_{medium}$, and $n_{high}$ correspond to refractive indices of choices at three different wavelengths of interest [44]. For a radial GRIN medium, the formula ($V_{GRIN}$) is modified to

$$V_{GRIN} = \frac{\Delta n_{medium}}{\Delta n_{low} - \Delta n_{high}} \qquad (2)$$

where $\Delta n$ corresponds to a spatial change in index which transmitting light experiences over a travel distance within the lens [31,39–42]. The formulae indicate that an optical medium with a lesser-sloped refractive index spectrum (i.e., lower dispersion and correspondingly lower chromatic aberration) has a greater Abbe number.

Figure 8(b) shows the magnitude of the Abbe numbers ($|V_{GRIN}|$) of the $GeSe_2$-$As_2Se_3$-PbSe-based radial GRIN glass-ceramic nanocomposite medium, along with those of its starting homogeneous glass ($|V_{Homo}|$) as well as other widely-available optical materials over three spectral ranges of short-wave, mid-wave, and long-wave IR [39]. The formula for $V_{Homo}$ indicates that a homogeneous medium exhibits a single value of $V_{Homo}$, while $V_{GRIN}$ is tunable by inducing $\Delta n_{low}$, $\Delta n_{medium}$, and $\Delta n_{high}$ into an optical medium. Typically, values of $\Delta n_{low}$, $\Delta n_{medium}$, and $\Delta n_{high}$ are very similar unless the microstructure of a material undergoes a massive spatial variation through addition, removal or diffusion of elements [31,39–41]. Due to the similarity of the values, the denominator in the formula for $V_{GRIN}$ is very small. Hence, $|V_{GRIN}|$ increases significantly with a change of the numerator (i.e., by controlling $\Delta n_{medium}$), indicating that the formation of a GRIN profile ($\Delta n_{medium}$ = finite) in an originally homogeneous ($\Delta n_{medium} = 0$) medium leads to the significant increase in $|V_{GRIN}|$ and reduction of the medium's chromatic aberration. The orders of magnitude increase in $|V_{GRIN}|$ of a $GeSe_2$-$As_2Se_3$-PbSe medium observed in Fig. 8(b) clearly shows that the chromatic aberration of the GRIN glass-ceramic nanocomposite medium is far less than that of its counterpart starting homogeneous glass medium.

## 4. Refractive and diffractive optical elements for the midwave infrared (MIR)

Today's legacy lenses are predominantly based on an optically homogeneous media [44]. While there has been steady improvement of manufacturing techniques such as computer numerical control and precision glass molding, the utilization of spherical or aspheric monolithic bulk materials with fixed refractive indices is still a key fabrication route. Since such materials focus different wavelengths at varying distances from the lenses, homogeneous lenses inherently suffer from chromatic aberration [44]. Common solutions to this lingering issue include the double-Gauss lens where multiple lenses with different shapes and refractive indices are stacked together to correct the trajectory of transmitting lights with different wavelengths, as illustrated in Fig. 9(a). However, these constituent lenses are typically made of heavy crystalline materials, leading to the significant increase in the size, weight, power consumption, and cost (SWAP-C) of imaging systems [42,44].

Nature provides a wide variety of materials with different structures and functions. The observation of the biological world often allows us to translate its design into the technical world including optics [45]. For example, the lens of the human eye has a spatially varying mass density, leading to the formation of a gradient refractive index (GRIN) profile [46–48], as shown in Fig. 9(b). Such a GRIN profile desirably guides the trajectory of incoming lights, thereby minimizing the chromatic aberration and allowing the eye to image objects with good resolution. This unique structure-property relationship observed in living organisms gave birth to bio-inspired optics.

The key strategic advantages of GRIN lenses include: 1) a single lens can correct the chromatic aberration, 2) the lens can be shaped into a wide range of geometry including a flat one, and 3) it enables the design of novel imaging systems with minimized size and even previously uncharted novel optical functions. Since the creation of Wood's GRIN lens, a wide range of experimental methods to induce GRIN profiles in optical media have been proposed for applications in
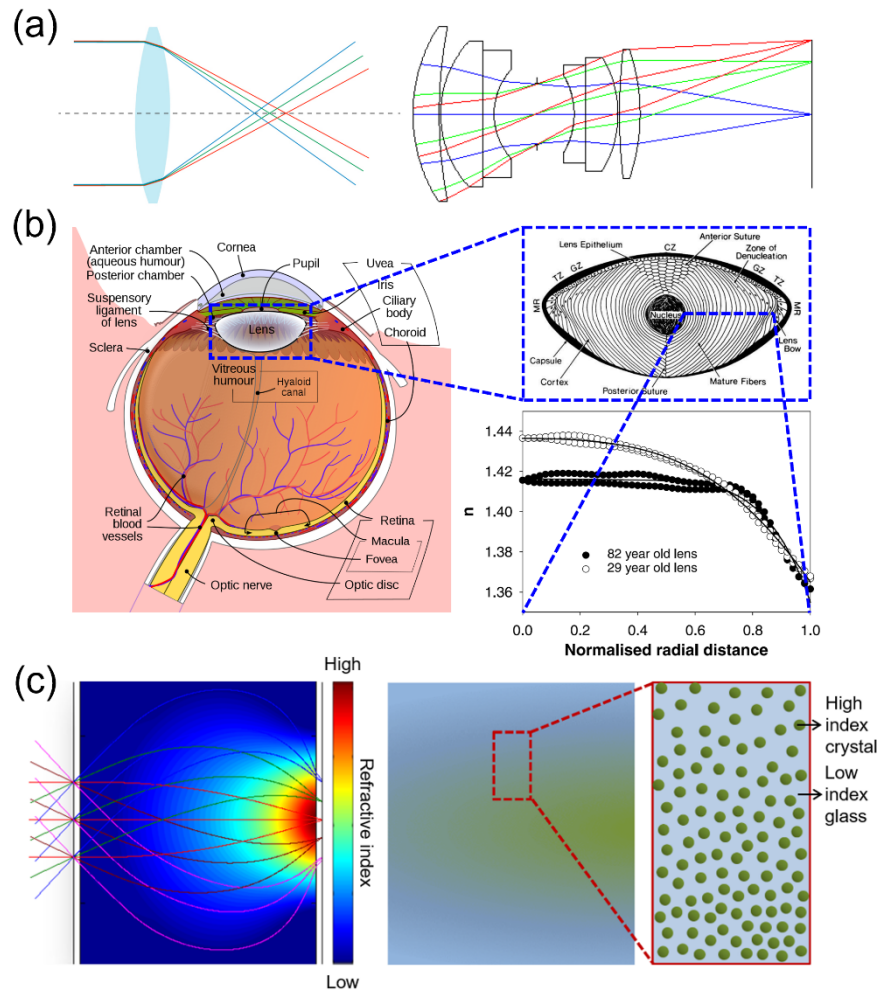
**Fig. 9.** (a) Chromatic aberration caused by a traditional single-component lens with a fixed value of refractive index and a double-Gauss lens configuration with multiple corrective lenses [44]. (b) The anatomy of a human eye, a close view of a lens in the human eye, and the spatially-varying refractive index profile of the lens [46–48]. (c) A nanocomposite-based biomimetic flat GRIN lens and a method to create a GRIN profile through the formation of high refractive index crystals within a low refractive index glass matrix [38]. (b) Adapted from [46] (open source). Adapted with permission from [47]. © 2011 IOP Publishing and [48]. © 2002 Elsevier Publishing.

the visible and infrared (IR) ranges. Thanks to the recent development of desirable starting materials and post modification process methods to spatially tailor refractive index profiles, the manufacturability of GRIN materials has been increasingly feasible. Key pre-requisites for the choice of starting materials and post modification processes include 1) an ability to spatially tailor a refractive index profile in a three-dimensional (3-D) volume, 2) an ability to scale up the formation of a GRIN profile in the entire volume of a target material to maximize a resulting optical path difference (OPD) of propagating light [$= \int n(t) dt$ where $n(t)$ corresponds to a value of refractive index at a depth of $t$], and 3) an ability to minimize microstructural defects, thereby maintaining a resulting GRIN medium's optical transparency.

One of key methods to induce GRIN profile into optical media is to utilize a described above crystallization process which converts a starting homogeneous glass to a glass-ceramic nanocomposite consisting of co-existing high refractive index crystalline phases and low index amorphous phases [38,1]. A nanocomposite with co-existing sub-wavelength phases can be approximated as an effective medium, and its effective refractive index is formulated by

$$n_{\text{effective}} \approx \sum_{i=1}^{N}(V_{i_{\text{th phase}}} \times n_{i_{\text{th phase}}}) \tag{3}$$

where $n$ and $V$ correspond to the refractive index and volume fraction of each phase within a nanocomposite, respectively. The formulation indicates that spatial variation in the volume fraction of high refractive index crystalline phases leads to a transmissive effective medium with a GRIN profile. Figure 9(c) illustrates such an example where the volume fraction of high refractive index nanoparticles (green) is spatially varied within a low refractive index matrix (blue), which gives rise to the formation of a single-component flat GRIN medium where propagating light is guided along curved trajectories [1,38].

To demonstrate the applicability of our material-process combination and realize optically functional components, we created a diffraction grating structure within a $GeSe_2$-$As_2Se_3$-PbSe film and characterized its optical performance [31]. Specifically, we utilized the photo-thermal process in a laterally-discrete fashion to induce the spatially-modulated refractive index within the film. This is enabled by the insertion of a grayscale optical mask with a spatially-modulated transparency which correspondingly allows the incident laser beam to reach the surface of the target film in a laterally discrete fashion. Due to spatially-alternating laser-exposed and unexposed regions within the film, a post heat treatment of the film leads to the formation of a structure which consists of spatially-alternating glass-ceramic and amorphous regions, thereby creating a grating structure with spatially-alternating high and low refractive index regions. Figure 8(c) illustrates the schematic of the grating structure under a transmission mode, along with diffraction spots formed at a detector upon the diffraction of 2 μm plane waves through the structure. The diffraction spots indicate the existence of a grating structure and can be quantitatively analyzed to identify a difference in refractive indices of glass-ceramic and amorphous regions within the grating structure. Using the diffraction equation [31], the difference is calculated to be 0.077, consistent with a value of 0.080 which was targeted through a combination of specific laser exposure and post heat treatment parameters. The value of the difference itself and its consistency with the targeted value confirm the ability for the photo-thermal process to induce complex spatial profiles of the refractive index. Ultimately, this demonstration suggests the applicability of the material-process combination for a wide variety of IR applications based on spatially-tailored refractive index profiles.

The three dimensional (3D) modification of refractive index in optical media can significantly decrease the size and cost of imaging systems. We foresee that by utilizing tightly-focused nanosecond pulsed laser exposure, both high spatial selectivity and resolution would not only be facilitated in the lateral direction but also in the axial direction, thereby realizing full 3D control of refractive index within $GeSe_2$-$As_2Se_3$-PbSe media. The potential route to tailoring 3D refractive index distributions would reveal further insight into a mechanistic origin behind light-matter interactions and pave the way toward previously uncharted novel IR functionalities. While the novel photo-thermal process was mainly demonstrated for $GeSe_2$-$As_2Se_3$-PbSe chalcogenide materials, the process and its variants are expected to be applicable to a wide range of IR materials where high refractive index sub-wavelength phases can be systematically created by such laser-based material modification processes.

## 5. Diffractive optical elements for UV, visible and IR

It has been shown above that photo-thermo-induced refractive index change in PTR glass enables recording phase volume holograms with high efficiency. A volume holographic optical element is an interference pattern recorded in a *volume* of a photosensitive medium by means of refractive index modulation. The simplest volume holographic element is a volume Bragg grating which is a system of planar layers with a modified refractive index. Depending on diffraction angle and orientation of a grating in the plate, one can distinguish several types of Bragg gratings. A transmitting volume Bragg grating is a diffractive optical element operating in a transmitting geometry, when a diffracted beam crosses the back surface of the grating. Grating is called a reflecting Bragg grating if diffracted beam crosses the front surface, and prismatic - if diffracted beam crosses one of the side surfaces. Bragg gratings in PTR glass were recorded by an exposure to the interference pattern of radiation of He-Cd laser operating at 325 nm. Grating periods ware varied from 0.1 to 200 μm. Volume gratings in both transmitting and reflecting mode were recorded with thickness ranged from 0.5 mm to 50 mm. Both transmitting and reflecting gratings could be tilted inside a glass plate for almost arbitrary angles. Diffraction efficiency was measured at different wavelengths ranged from 355 to 2000nm. In all cases, the maximum absolute diffraction efficiency of PTR Bragg gratings exceeded 95% while relative diffractive efficiency was demonstrated above 99.9999%.

An example of the angular selectivity of a transmitting PTR grating is shown in Fig. 10 [49].
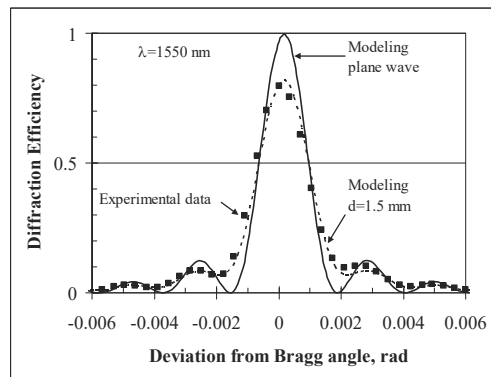


**Fig. 10.** Angular selectivity of transmitting PTR Bragg grating at 1550 nm. Period 1.42 μm, refractive index modulation 640 ppm, thickness 1.16 mm [49].

It was found that the experimental profiles of diffraction efficiency coincided with theoretical functions for the uniform sinusoidal Bragg grating within fluctuations which did not exceed 5%. One can see that angular selectivity of about 2 mrad is achieved in the PTR Bragg grating having thickness of 1 mm. It is important to note that some discrepancy between the model and experimental data are caused not by distortions of a PTR grating but by diffraction limited divergence of a laser beam with an aperture of 1.5 mm. Thus, transmitting PTR Bragg gratings can have angular selectivity comparable and even narrower than angular divergence of single-mode laser radiation. Actual angular selectivity of transmitting gratings can be narrowed down to tens of microradians that enables the creation of spatial filters operating in collimated beams. Switching of an incident beam between maximum (the one) and the zeros in Fig. 10 would result in switching of an exit beam between incident and diffracted angles which is angular magnification. Illumination of a grating with different wavelengths in maxima and minima of the diffraction spectra enables spectral combining of laser beams.

An example of spectral selectivity of a reflecting PTR grating is shown in Fig. 11 [50]. Deflection angles could be ranged from 120 to 180°, angular selectivity from 10 to 100 mrad,

spectral selectivity from 0.01 to 2 nm. Absolute diffraction efficiency up to 98.5% and relative diffraction efficiency for plane wave of 99.9999% were demonstrated. An example in Fig. 11 shows a spectral scan of a reflecting grating for an incident angle of 3.8°. One can see that spectral width (FWHM) of this filter coincides with the theoretical value within accuracy of few percent. Some discrepancy is caused by finite divergence of the used probe beam which was about 0.6 mrad. These gratings are used as notch filters, especially for Raman spectroscopy [51] and as resonant feedback for laser resonators [52,53].
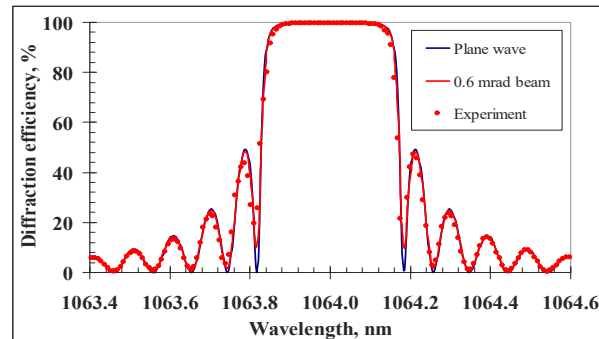


**Fig. 11.** Spectral selectivity of reflecting VBGs used for 5-channel SBC with 0.43 nm channel spacing [50].

There are some tasks that require wide spectral selectivity of filters or specific dependence of a position of a reflection plane on wavelength. Reflecting Bragg gratings with gradually varied period (chirped gratings) in PTR glass has been recorded (Fig. 12) [54]. Both transmitted and diffracted beams have been measured simultaneously while wavelength was swept. Reflection spectra of a chirped PTR Bragg grating with spectral width of 12 nm and diffraction efficiency exceeding 90% were obtained. Such gratings could be used for stretching and compression of high power short laser pulses.

An important feature of PTR technology is an opportunity to record a number of diffractive gratings in the same volume of glass. Each hologram is independent as no refractive changes of refractive index and, therefore, no writing beam diffraction occur in the process of recording. All
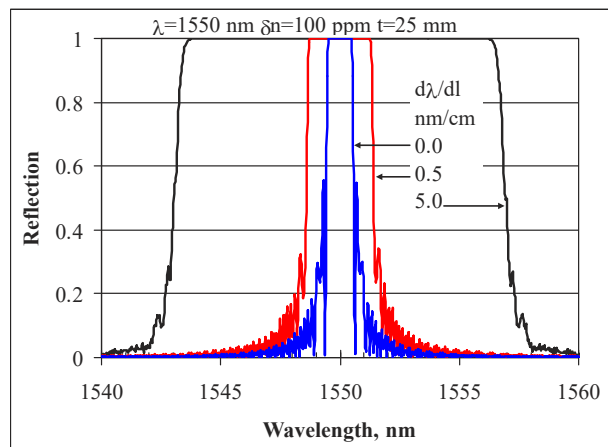


**Fig. 12.** Spectral selectivity of chirped reflecting VBGs used laser pulses stretching and compression [54].

holograms appear only in the process of thermal development. Capacity for multiple hologram recording is determined by the maximum of refractive index modulation. Thus, for the near IR region phase incursion enough for 100% diffraction efficiency can be achieved in a thickness about 1 mm. This means that PTR glass wafer of 5 mm can include up to 5 diffractive gratings with high diffraction efficiency. Experimentally, pairs of 98% at 1550 nm transmitting gratings were recorded in 3 mm PTR glass wafers (Fig. 13). For low efficiencies a high number of Bragg gratings can be realized in thin glasses. Theoretical estimations show that it is possible to record in the same PTR glass slab up to several thousands of gratings. This feature is used for complex beam splitters and could be a basis for archive data storage.
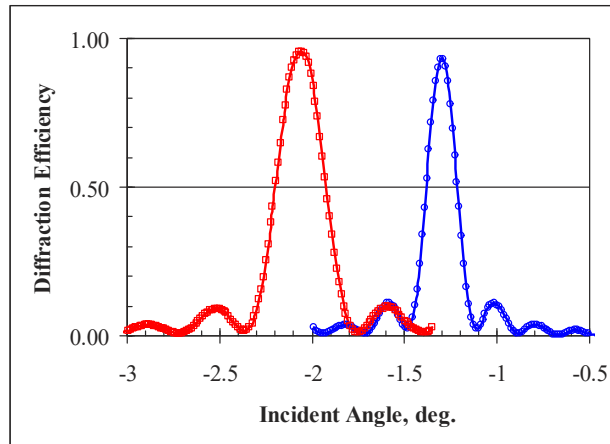


**Fig. 13.** Angular selectivity of transmitting VBGs recorded in the same volume of PTR glass [49].

   As shown above, PTR glass co-doped by sensitizers and luminescent agents provides both photosensitivity and optical gain. Therefore, reflecting VBGs were recorded in PTR glasses co-doped with Nd and Yb. Two geometries were used for lasing demonstration (Fig. 14) [55].
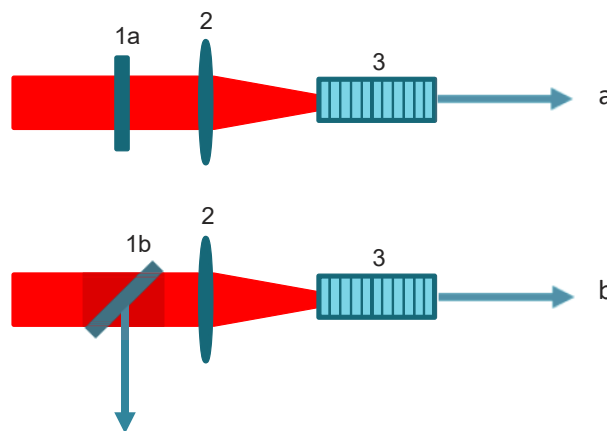


**Fig. 14.** Experimental setups of a distributed Bragg reflector (DBR) (a) and distributed feedback (DFB) (b) lasers. 1 – dichroic mirror with high transmission for pumping radiation and high reflection for signal at normal incidence (a) or at 45° (b), 2 – lens, 3 – Nd or Yb doped PTR glass slab with 99% diffraction efficiency Bragg mirror.

The first one is a distributed Bragg reflector where a resonator includes a high reflecting dichroic mirror and an output coupler that is an Yb or Nd doped PTR glass slab with a narrowband reflecting Bragg grating operating at a wavelength corresponding to maximum of luminescence band of a dopant.

In figure 14(a) pumping is produced through the dichroic mirror. The second is a monolithic device with distributed feedback where includes only the VBG co-doped with Nd or Yb. It was found that Yb-doped DFB laser provides a single-frequency operation with spectral width <250 kHz. This monolithic laser cannot be misaligned, and has high tolerance to shocks and vibrations.

To demonstrate an opportunity for complex hologram recording for the visible region, a Tb-doped PTR glass was used [56]. The sample was illuminated by three beams (Fig. 15). The first beam at 375 nm produces excitation of Tb to a metastable level. A concurrent irradiation with two interfering beams at 532 nm produces ionization of Tb and triggers a chain of structural transformation resulted in refractive index change. The lower beam is a just collimated laser beam. The upper beam is focused by a two-lens system. The photo of a focal spot produced by this system is shown in Fig. 15(a). The exposed glass sample was developed with a standard procedure and illuminated by the low 532 nm beam. The photo of a focal spot is shown in Fig. 15(b). One can see that both spots are identical. It should be noted that rotation of the plate in the plane of the figure for 180° converts it to the negative lens with the same focal length.
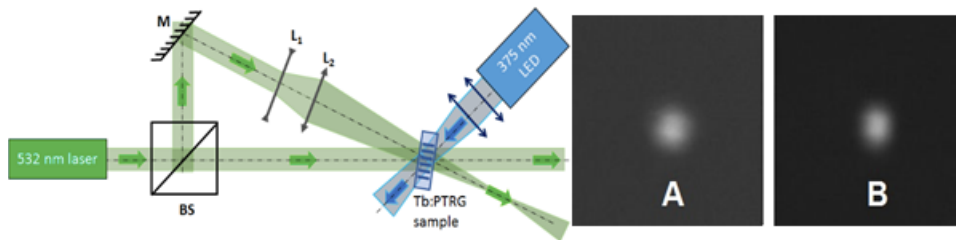


**Fig. 15.** Left: experimental setup for recording holographic lens in $Tb^{3+}$ doped PTR glass (BS – beamsplitter, M – mirror, $L_1$, $L_2$ – lenses). Right: photos of spots in focal plane of an original lens system $L_1$-$L_2$ (A) and a holographic lens (B).

One more example of a complex hologram operating in wide spectral range is a holographic phase mask [57]. Phase masks are optical components that provide a specified profile of
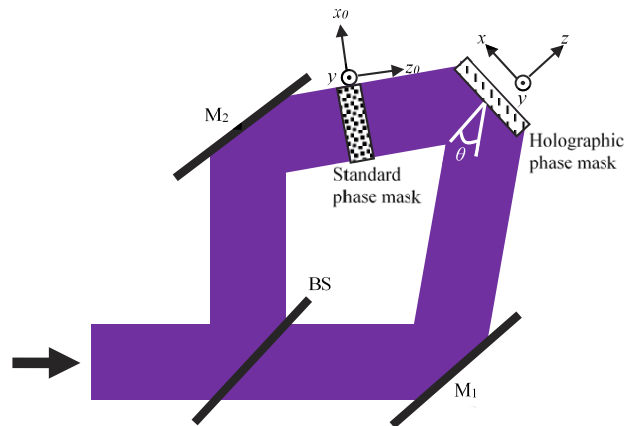


**Fig. 16.** Experimental setup for hologram of phase mask recording. BS – beam splitter, $M_1$ and $M_2$ – mirrors.

optical path (*n×t*) across the aperture and enable transformation between different spatial modes. Conventional phase masks are fabricated by spatial profiling of thickness or refractive index. It is clear that such devices are monochromatic because the transform function is determined by profile measured in fractions of wavelength. It was shown in Ref. [57] that placing a conventional phase mask in an interferometer for hologram grating recording (Fig. 16) results in incorporation of this mask to a volume Bragg grating.

It is important that phase profile of a beam diffracted by the recorded grating is the same as in the master phase mask for any wavelength. This means that contrary to conventional phase masks, a holographic phase mask is tunable (Fig. 17). Moreover, it was found that holographic phase masks could be made achromatic [58]. This feature enables spatial transformation of broadband
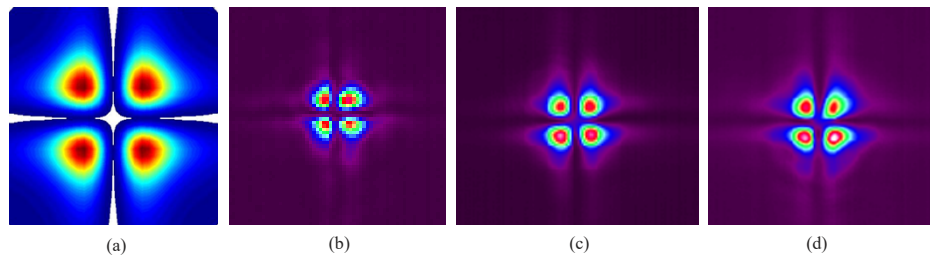


(a)                    (b)                    (c)                    (d)

**Fig. 17.** (a) Simulated far field profile of a beam after passing through an ideal four-sector binary mask and the diffracted beam from a four-sector holographic phase mask at (b) 632.8 nm, (c) 975 nm, and (d) 1064 nm.
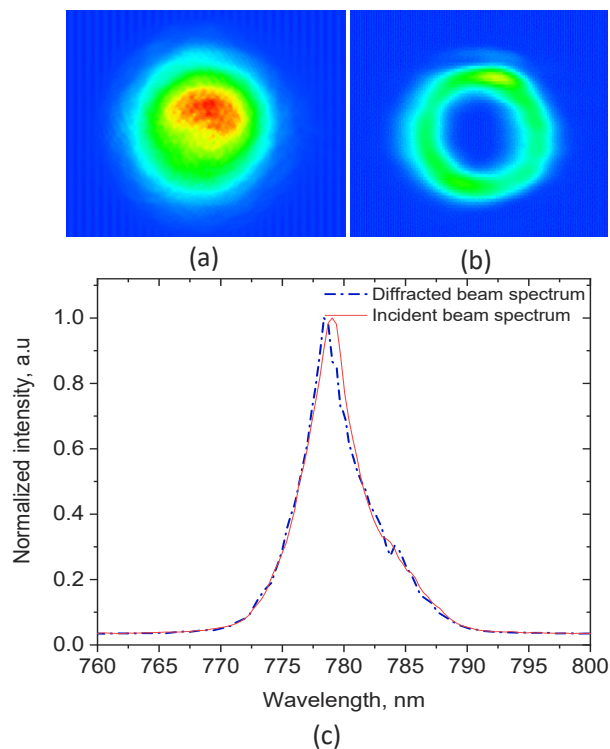


(a)                              (b)



(c)

**Fig. 18.** Conversion of a 70 fs Gaussian beam at 780 nm to a vortex one. (a) Incident beam profile, (b) diffracted vortex beam profile, (c) incident and diffracted beams spectra.

laser beams, e.g. femtosecond ones (Fig. 18). Thus, holographic phase masks are new optical elements that provide unprecedented opportunities for spatial transformation of laser beams.

## 6.　Summary

Silicate and chalcogenide glasses have been created that demonstrate photoinduced refractive index change resulting from crystalline phase precipitation after glass exposure to optical radiation followed by thermal treatment. These materials enable fabrication of refractive and diffractive optical elements operating from near UV to long wavelength IR spectral region. Such optical elements can be created by these materials and methods resulting in components such as lenses, diffraction gratings, spatial and spectral filters, laser pulse stretchers and compressors, and holographic phase masks. Such materials and optical components pave the way for new optical systems operating in extremely wide spectral ranges.

**Disclosures.** The authors declare no conflicts of interest.

**Data availability.** Data underlying the results presented in this paper are available in the associated references or are available upon reasonable request of the authors.

## References

1. K. Richardson, M. Kang, L. Sisken, A. Yadav, C. Blanco, M. Antia, A. Lepicard, M. Dussauze, C. Schwarz, C. Pantano, C. Rivero-Baleine, A. Kirk, S. Mensah, M. Driggers, S. Kuebler, C. Grabill, S. Novak, C. Li, W. Deng, J. Hu, P.-T. Lin, A. Agarwal, T. Mayer, A. Pogrebnyakov, and A. Swisher, "Advances in Infrared GRIN: a review of novel materials towards components and devices," Proc. SPIE **10627**(9), 9 (2018).
2. S. D. Stookey, "Photosensitive glass," Ind. Eng. Chem. **41**(4), 856–861 (1949).
3. V. A. Borgman, L. B. Glebov, N. V. Nikonorov, G. T. Petrovskii, V. V. Savvin, and A. D. Tsvetkov, "Photothermal refractive effect in silicate glasses," Soviet Physics Dokl. **34**(11), 1011–1013 (2016).
4. L. B. Glebov, N. V. Nikonorov, E. I. Panysheva, G. T. Petrovskii, V. V. Savvin, I. V. Tunimanova, and V. A. Tsekhomskii, "Polychromatic glasses - a new material for recording volume phase holograms," Soviet. Physics. Dokl. **35**, 878–880 (1990).
5. O. M. Efimov, L. B. Glebov, L. N. Glebova, K. C. Richardson, and V. I. Smirnov, "High-Efficiency Bragg Gratings in Photothermorefractive Glass," Appl. Opt. **38**(4), 619–627 (1999).
6. T. Cardinal, O. M. Efimov, H. G. Francois-Saint-Cyr, L. B. Glebov, L. N. Glebova, and V. I. Smirnov, "Comparative study of photo-induced variations of X-ray diffraction and refractive index in photo-thermo-refractive glass," J. Non-Cryst. Solids **325**(1-3), 275–281 (2003).
7. L. Glebov, "Fluorinated silicate glass for conventional and holographic optical elements," Proc. SPIE **6545**, 654507 (2007).
8. J. Lumeau and L. B. Glebov, "Modeling of the induced refractive index kinetics in photo-thermo-refractive glass," Opt. Mater. Express **3**(1), 95–104 (2013).
9. J. Lumeau, L. Glebova, and L. B. Glebov, "Evolution of absorption spectra in the process of nucleation in photo-thermo-refractive glass," Adv. Mater. Res. **39-40**(40), 395–398 (2008).
10. J. Lumeau, L. Glebova, V. Golubkov, E. D. Zanotto, and L. B. Glebov, "Origin of crystallization-induced refractive index changes in photo-thermo-refractive glass," Opt. Mater. **32**(1), 139–146 (2009).
11. J. Lumeau and E. D. Zanotto, "A review of the photo-thermal mechanism and crystallization of photo-thermo-refractive (PTR) glass," Int. Mater. Rev. **62**(6), 348–366 (2017).
12. L. B. Glebov, "Kinetics modeling in photosensitive glass," Opt. Mater. **25**(4), 413–418 (2004).
13. O. M. Efimov, L. B. Glebov, and H. P. Andre, "Measurement of the induced refractive index in a photo-thermo-refractive glass by a liquid-cell shearing interferometer," Appl. Opt. **41**(10), 1864–1871 (2002).
14. S. R. Nersisyan, N. V. Tabiryan, and C. M. Stickley, "Characterization of glass and high-power near-infrared CW laser beams using nonlinear optical techniques," Opt. Eng. **45**(10), 104301 (2006).
15. K. Chamma, J. Lumeau, L. Glebova, and L. B. Glebov, "Generation and bleaching of intrinsic color centers in photo-thermo-refractive glass matrix," J. Non-Cryst. Solids **356**(44-49), 2363–2368 (2010).
16. J. Lumeau, L. Glebova, and L. B. Glebov, "Investigation of the induced absorption and scattering in visible and NIR ranges in photo-thermo-refractive glass," in International Congress on Glass (2007), paper M3
17. A.V. Dotsenko, L.B. Glebov, and V.A. Tsekhomsky, *Physics and Chemistry of Photochromic Glasses* (CRC Press, 1998).
18. J. Lumeau, L. Glebova, and L. B. Glebov, "Absorption and scattering in photo-thermo-refractive glass induced by UV-exposure and thermal development," Opt. Mater. **36**(3), 621–627 (2014).

19. M. Anne, J. Lumeau, L. Glebova, and L. B. Glebov, "Specific absorption spectra of cerium in multicomponent silicate glasses," J. Non-Cryst. Solids **356**(44-49), 2337–2343 (2010).

20. J. Lumeau, A. Sinitskiy, L. N. Glebova, L. B. Glebov, and E. D. Zanotto, "Spontaneous and photo-induced crystallization of PTR glass," Phys. Chem. Glasses: Eur. J. Glass Sci. Technol. B **48**(4), 281–284 (2007).

21. L.B. Glebov and V.I. Smirnov, "Interaction of photo-thermo-refractive glass with nanosecond pulses at 532 nm," Proc. SPIE **5273**, 396–401 (2004).

22. P. S. Shirshnev, R. A. Alvarez, and L. B. Glebov, "Long-wavelength optical absorption edge of photo-thermo-refractive glass," Opt. Mater. Express **11**(9), 2883–2891 (2021).

23. L.B. Glebov, "High brightness laser design based on volume Bragg gratings," Proc. SPIE **6216**, 621601 (2006).

24. O.M. Efimov, L.B. Glebov, S. Papernov, and A.W. Schmid, "Laser-induced damage of photo-thermo-refractive glasses for optical-holographic-element writing," Proc. SPIE **3578**, 564–575 (1999).

25. S. Santran, M. Martinez-Rosas, L. Canioni, L. Sarger, L. N. Glebova, A. Tirpak, and L. B. Glebov, "Nonlinear refractive index of photo-thermo-refractive glass," Opt. Mater. **28**(4), 401–407 (2006).

26. L. Glebova, J. Lumeau, and L. B. Glebov, "Photo-thermo-refractive glass co-doped with $Nd^{3+}$ as a new laser medium," Opt. Mater. **33**(12), 1970–1974 (2011).

27. N. Khaldoon, V. Aseev, S. Ivanov, A. Ignatiev, and N. Nikonorov, "Optical, spectroscopic properties and Judd–Ofelt analysis of $Nd^{3+}$-doped photo-thermo-refractive glass," J. Lumin. **213**, 255–262 (2019).

28. N. Khaldoon, V. Aseev, S. Ivanov, A. Ignatiev, and N. Nikonorov, "Spectroscopic and laser properties of erbium and ytterbium co-doped photo-thermo-refractive glass," Ceram. Int. **46**(16), 26282–26288 (2020).

29. F. Kompan, G. Venus, L. Glebova, H. Mingareev, and L. Glebov, "Photo-thermo-refractive glass with sensitivity to visible and near IR radiation," Opt. Mater. Express **6**(12), 3881–3891 (2016).

30. B. J. Eggleton, B. Luther-Davies, and K. Richardson, "Chalcogenide photonics," Nat. Photonics **5**(3), 141–148 (2011).

31. M. Kang, A. M. Swisher, A. V. Pogrebnyanov, L. Liu, A. Kirk, S. Aiken, L. Sisken, C. Lonergan, J. Cook, T. Malendevych, F. Kompan, I. Divliansky, L. B. Glebov, M. C. Richardson, C. Rivero-Baleine, C. G. Pantano, T. S. Mayer, and K. Richardson, "Ultra-low dispersion multicomponent thin film chalcogenide glass for broadband gradient index optics," Adv. Mater. **30**(39), 1803628 (2018).

32. M. Kang, T. Malendevych, G. Yin, I. B. Murray, M. C. Richardson, J. Hu, I. Mingareev, and K. Richardson, "Scalable laser-written Ge-As-Pb-Se chalcogenide glass-ceramic films and the realization of infrared gradient refractive index elements," Proc. SPIE **10998**, 13 (2019).

33. I. Mingareev, M. Kang, M. Truman, J. Qin, G. Yin, J. Hu, C. M. Schwarz, I. B. Murray, M. C. Richardson, and K. A. Richardson, "Spatial tailoring of the refractive index in infrared glass-ceramic films enabled by direct laser writing," Opt. Laser Technol. **126**, 106058 (2020).

34. I. Mingareev, M. Kang, T. Malendevych, G. Yin, J. Hu, K. Richardson, and M. Richardson, "Laser-induced modification of local refractive index in infrared glass-ceramic films," Proc. SPIE **10906**, 33 (2019).

35. A. Apling, A. J. Leadbetter, and A. C. Wright, "A comparison of the structures of vapour-deposited and bulk arsenic sulphide glasses," J. Non-Cryst. Solids **23**(3), 369–384 (1977).

36. A. V. Belykh, O. M. Efimov, L. B. Glebov, Y. A. Matveev, A. M. Mekryukov, M. D. Mikhailov, and K. A. Richardson, "Photo-structural transformation of chalcogenide glasses under non-linear absorption of laser radiation," J. Non-Cryst. Solids **213-214**, 330–335 (1997).

37. K. Shimakawa, A. V. Kolobov, and S. R. Elliott, "Photoinduced effects and metastability in amorphous semiconductors and insulators," Adv. Phys. **44**(6), 475–588 (1995).

38. K. Richardson, M. Kang, L. Sisken, A. Yadav, S. Novak, A. Lepicard, I. Martin, H. Francois-Saint-Cyr, C. M. Schwarz, T. S. Mayer, C. Rivero-Baleine, A. J. Yee, and I. Mingareev, "Advances in infrared GRIN materials: a review," Opt. Eng. **59**(11), 1 (2020).

39. M. Kang, L. Sisken, C. Lonergan, A. Buff, A. Yadav, C. Goncalves, C. Blanco, P. Wachtel, J. D. Musgraves, A. V. Pogrebnyakov, E. Baleine, C. Rivero-Baleine, T. S. Mayer, C. G. Pantano, and K. A. Richardson, "Monolithic chalcogenide optical nanocomposites enable infrared system innovation: gradient refractive index (GRIN) optics," Adv. Opt. Mater. **8**(10), 2000150 (2020).

40. L. Sisken, M. Kang, J. M. Veras, C. Smith, A. Buff, A. Yadav, D. McClane, C. Blanco, C. Rivero-Baleine, T. S. Mayer, and K. Richardson, "Infrared glass ceramics with multi-dispersion and gradient refractive index attributes," Adv. Funct. Mater. **29**(35), 1902217 (2019).

41. M. Kang, I. Martin, R. Sharma, C. Blanco, S. Antonov, T. J. Prosa, D. J. Larson, H. Francois-Saint-Cyr, and K. A. Richardson, "Unveiling true 3-d nanoscale microstructural evolution in chalcogenide nanocomposites: a roadmap for advanced infrared functionality," Adv. Opt. Mater. **9**(9), 2002092 (2021).

42. D. T. Moore, "Gradient-index optics: a review," Appl. Opt. **19**(7), 1035–1038 (1980).

43. D. Gibson, S. S. Bayya, V. Q. Nguyen, J. D. Myers, E. F. Fleet, J. S. Sanghera, J. Vizgaitis, J. P. Deegan, and G. Beadie, "Diffusion-based gradient index optics for infrared imaging," Opt. Eng. **59**(11), 1 (2020).

44. E. Hecht, *Optics* (Addison-Wesley, 1998).

45. G. Zuccarello, D. Scribner, R. Sands, and L. J. Buckley, "Materials for Bio-inspired Optics," Adv. Mater. **14**(18), 1261–1264 (2002).

46. R.H. Castilhos, Diagram of the Human eye in English, Wikipedia (2007), https://en.wikipedia.org/wiki/Iris_(anatomy)#/media/File:Schematic_diagram_of_the_human_eye_en.svg

47. P. Nogueira, M. Zankl, H. Schlattl, and P. Vaz, "Dose conversion coefficient for monoenergetic electrons incident on a realistic human eye model with different lens cell populations," Phys. Med. Biol. **56**(21), 6919–6934 (2011).

48. B. A. Moffat, D. A. Atchison, and J. M. Pope, "Age-related changes in refractive index distribution and power of the human lens as measured by magnetic resonance micro-imaging in vitro," Vision Res. **42**(13), 1683–1693 (2002).

49. L. B. Glebov, "Volume holographic elements in a photo-thermo-refractive glass," Jnl. of Holography and Speckle **5**(1), 77–84 (2009).

50. O. Andrusyak, V. Rotar, A. Sevian, V. Smirnov, G. Venus, and L.B. Glebov, "Spectral stabilization of diode bar by volume bragg grating incorporated in fast axis collimator," in *Proceedings of Solid State and Diode Lasers Technical Review* (2007), paper BC2-2.

51. A.L. Glebov, O. Mokhun, A. Rapaport, S. Vergnole, V. Smirnov, and L.B. Glebov, "Volume Bragg gratings as ultra-narrow and multiband optical filters," Proc. SPIE **8428**, 84280C (2012).

52. L. Glebov, "High-performance solid-state and fiber lasers controlled by volume Bragg gratings," Reza Kenkyu **41**(9), 684–690 (2013).

53. L. Glebov, "High brightness diode lasers controlled by volume Bragg gratings," Proc. SPIE **10123**, 1012319 (2017).

54. L. Glebov, V. Smirnov, E. Rotari, I. Cohanoschi, L. Glebova, O. Smolski, J. Lumeau, C. Lantigua, and A. Glebov, "Volume-chirped Bragg gratings: monolithic components for stretching and compression of ultrashort laser pulses," Opt. Eng. **53**(5), 051514 (2014).

55. A. Ryasnyanskiy, N. Vorobiev, V. Smirnov, J. Lumeau, L. Glebova, O. Mokhun, Ch. Spiegelberg, M. Krainak, A. Glebov, and L. Glebov, "DBR and DFB lasers in neodymium- and ytterbium-doped photo-thermo-refractive glasses," Opt. Lett. **39**(7), 2156–2159 (2014).

56. F. Kompan, I. Divliansky, V. Smirnov, and L. Glebov, "Holographic lens for 532 nm in photo-thermo-refractive glass," Opt. Laser Technol. **105**, 264–267 (2018).

57. M. SeGall, I. Divliansky, C. Jollivet, A. Schülzgen, and L.B. Glebov, "Holographically encoded volume phase masks," Opt. Eng. **54**(7), 076104 (2015).

58. N. Mohammadian, O. Mhibik, M. SeGall, S. Yaraghi, L. Glebov, and I. Divliansky, "Versatile approach to laser beam shaping and analyzing by holographic phase masks," J. Opt. **23**(11), 115609 (2021).